Accepted Article

Title: Operando Spectroscopic Insights into CO2 Reduction at Electrode/Polyelectrolyte Interfaces

Authors: Jieyu Wang, Bing Huang, Li Xiao, Gongwei Wang, and Lin Zhuang

Operando Spectroscopic Insights into CO$_2$ Reduction at Electrode/Polyelectrolyte Interfaces

Jieyu Wang, Bing Huang, Li Xiao, Gongwei Wang[*], Lin Zhuang[*]

College of Chemistry and Molecular Sciences, Hubei Key Lab of Electrochemical Power Sources, Wuhan University, Wuhan 430072, China

[*]*Corresponding e-mails: gwwang@whu.edu.cn, lzhuang@whu.edu.cn*

Abstract

The electrode/polyelectrolyte interface is a notable feature in modern electrochemical technologies that utilize membrane electrode assembly (MEA) configurations. However, its interfacial structure and catalytic behavior remain poorly understood. Here we developed an integrated *operando* Raman spectroscopy and mass spectrometry (MS) method, to directly investigate the CO_2 reduction mechanism at the electrode/polyelectrolyte interface within a practical MEA electrolyzer operating at high current densities. Combined with isotope labeling experiments and ab initio molecular dynamics (AIMD) simulations, we provide, for the first time, the direct spectroscopic evidence of *CCO, a crucial intermediate for C_2 product formation, which has been frequently hypothesized but rarely detected in previous studies. By contrast, the linearly adsorbed $*CO_L$ intermediate, typically observed in conventional liquid electrolytes, was absent. These distinct behaviors arise from the unique structure of the electrode/polyelectrolyte interface, which shifts the rate-determining step from the usual C-C coupling to the *CCO hydrogenation in the conversion of CO_2 to C_2 products. This study not only deepens our understanding of electrode/polyelectrolyte interfacial characteristics, but also offers valuable insights for advancing the performance of CO_2 MEA electrolyzers.

Keywords: Electrode/polyelectrolyte interface, CO_2 reduction, *Operando* mechanism, Raman spectroscopy, Mass spectrometry

2

Introduction

Electrochemical technologies, such as fuel cells,[1,2] water splitting,[3,4] and CO_2 electrolysis,[5,6] offer significant promise for addressing the urgent challenges of large-scale renewable energy storage and carbon emission reduction. At the heart of these technologies is the electrode/electrolyte interface, where electrochemical reactions occur.[7] A thorough exploration of the interfacial structure and its impact on electrochemical processes is thus essential.[8] This understanding is crucial for the rational design of key materials, such as efficient electrode catalysts and electrolytes, and for advancing the performance of electrochemical technologies.[9] Early electrochemical studies primarily relied on electrical signals for both excitation and detection, through applying varying potentials/voltages or currents and observing the corresponding responses to probe the electrode/electrolyte interface.[10] Since the 1970s, the introduction of various spectroscopic techniques, such as electrochemical *in-situ* infrared and Raman spectroscopy, has enabled the acquisition of molecular- and atomic-scale information at the electrode/electrolyte interface during electrochemical testing,[11–13] significantly deepening our understanding of electrochemical interfaces and reaction mechanisms.

Nevertheless, it is important to note that most electrochemical *in-situ* spectroscopies developed to date focus on studying the electrode/liquid electrolyte interface. In contrast, modern electrochemical technologies increasingly employ polymer electrolytes (i.e., polyelectrolytes) instead of liquid electrolytes (e.g., $HClO_4$, KOH solution).[14] This shift enables the construction of zero-gap membrane electrode assembly (MEA) devices, which help reduce internal resistance and thus improve electrochemical energy conversion efficiency.[15] The inherent differences between polyelectrolytes and liquid electrolytes—such as variations in ionic species (organic *versus* inorganic) and ionic mobility (bound *versus* free)—inevitably result in significant differences in the microstructure and catalytic behavior at the electrode/polyelectrolyte interface compared to the conventional electrode/liquid electrolyte interface. For instance, our recent studies have shown that CO_2 reduction can occur at the electrode/polyelectrolyte interface with immobilized organic cations, a reaction that is challenging to achieve in liquid electrolytes containing free organic cations.[16,17]

Additionally, to facilitate spectroscopic detection, these widely used *in-situ* spectroscopies

3

often require specially designed electrochemical cells.[18] This often leads to a mismatch in the testing conditions between *in-situ* spectroscopic characterization and electrochemical performance evaluation, making it unreliable to correlate spectroscopic evidence with actual electrochemical behavior in mechanistic studies.[19] This issue is especially pronounced in practical polyelectrolyte-based MEA devices, where operating conditions—such as current density, temperature, pressure, and humidity—differ significantly from those of conventional liquid electrolyte systems. These variations in operating conditions can even lead to markedly different catalytic behaviors.[20,21] For instance, a previous study demonstrated that while the nonprecious Mn-Co catalyst shows inferior oxygen reduction reaction (ORR) performance compared to Pt/C in aqueous KOH electrolyte, this trend reverses in alkaline polyelectrolyte fuel cells (APEFCs) with gas diffusion electrodes (GDEs) operating at 60°C, due to differences in water content at the catalytic interfaces.[22] Therefore, there is an urgent need to develop *operando* spectroscopic methods that are compatible with the operating conditions of MEA devices, to more accurately reveal the structural characteristics and catalytic behavior of the electrode/polyelectrolyte interface under practical working conditions. Indeed, some progress has been made in probing the interfaces within practical MEA-type fuel cells and water electrolyzers, through the combined use of techniques such as X-ray absorption spectroscopy (XAS),[23] near-ambient pressure X-ray photoelectron spectroscopy (NAP-XPS),[24,25] infrared spectroscopy,[26,27] and Raman spectroscopy.[28,29] However, operando studies focusing on CO_2 MEA electrolyzers, particularly those operating in a polyelectrolyte/pure water medium without any liquid electrolytes, remain rather limited.

In this study, we develop an integrated *operando* Raman spectroscopy and mass spectrometry (MS) method using the MEA configuration, to investigate CO_2 reduction at the electrode/polyelectrolyte interface. This approach allows for the simultaneous detection of interfacially adsorbed intermediates and volatile products (such as CO, CH_4, C_2H_4, C_2H_5OH, and others) under industrial-scale current densities, providing molecular insights into the CO_2 reduction mechanism in practical MEA electrolyzers. Notably, unlike the linearly adsorbed *CO_L intermediate commonly observed in Cu-catalyzed CO_2 reduction in KOH or $KHCO_3$ aqueous electrolytes,[30] we are surprised to find that *CO_L is absent at the electrode/polyelectrolyte interface. Instead, through the combination of isotope labeling and ab

initio molecular dynamics (AIMD) simulations, we successfully detected and identified the presence of *CCO, a crucial intermediate for C_2 product formation, which has been frequently hypothesized but rarely detected in previous studies with conventional liquid electrolytes.[31] Furthermore, we reveal that the presence of *CCO intermediate is attributed to the unique electrode/polyelectrolyte interfacial structure, which facilitates the Eley-Rideal type hydrogenation pathways directly using interfacial hydrogen bonding water as the proton source, while hinders the Langmuir-Hinshelwood type hydrogenation pathway involving surface-adsorbed water (*H_2O).

Results and discussion

To compare the CO_2 reduction behavior at the electrode/polyelectrolyte interface with that at the conventional electrode/liquid electrolyte interface, we developed two types of spectroelectrochemical cells. Figure 1a is the setup for investigating the electrode/liquid electrolyte interface (photograph in Figure S1), which is similar to designs reported in previous studies.[32,33] The working electrode, a Cu GDE, was prepared by spray-coating Cu nanocatalysts onto a hydrophobic carbon paper substrate (Figure S2). The counter and reference electrodes were immersed in the electrolyte solution. The excitation laser passes through a quartz window and a thin layer of the electrolyte solution, allowing the Raman scattering signals at the electrode/liquid electrolyte interface to be collected (Figure S3a). Although this GDE-based setup significantly enhances CO_2 mass transport and allows for electrochemical testing at current densities exceeding 100 mA/cm^2, the high internal resistance between the working and counter electrode, due to their large separation distance, makes operation at higher current densities challenging. Additionally, at higher current densities (>300 mA/cm^2, vide infra), a large number of gas bubbles will form on the electrode surface, which can severely interfere with Raman signal collection.

Figure 1b and Figure S4 illustrate the *operando* Raman-MS cell designed in this study, based on the zero-gap MEA configuration. In this setup, the cathode was fabricated using the catalyst-coated membrane (CCM) process, in which the Cu nanocatalyst and QAPEEK ionomer (molecular structure shown in Figure 1b) were ultrasonically mixed and spray-coated onto an alkaline polyelectrolyte membrane (QAPPT, Figure S5) to form the cathode (Details in

5

Supporting Information). An IrO_2-coated Ti anode was tightly pressed against the opposite side of the QAPPT membrane. A hydrophobic carbon paper with pre-drilled small holes ($\phi \approx 100$ μm, Figure S6) was used as the gas diffusion layer, and a quartz optical window was installed at the cathode flow field. This design allows the excitation laser (with a spot diameter of approximately 1 μm) to pass through the flow field and small holes, reaching the cathode catalyst layer for Raman signal collection (Figure S3b). Notably, the cathodic incidence detection can effectively eliminate the interference of fluorescence signals from alkaline polyelectrolyte membranes (e.g., QAPPT in this study), which typically contain a large number of conjugated benzene-ring structures. In addition to the Raman characterization, a capillary sampling port was introduced at the cathode outlet for MS analysis. This setup enables the collection of reaction intermediate information at the cathode interface by Raman and the simultaneous analysis of corresponding volatile products by MS for the CO_2 MEA electrolyzer under its normal operating conditions.
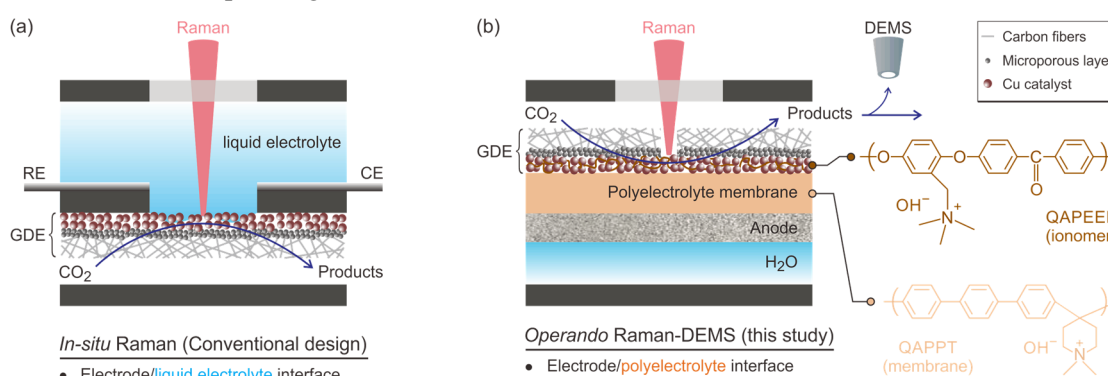

Figure 1. Schematic illustration of the *in-situ* and *operando* cells designed for studying CO_2 reduction. (a) *In-situ* Raman cell used for investigating the conventional electrode/electrolyte interface. The working electrode was a Cu GDE, and the electrolyte was a 1 M $KHCO_3$ aqueous solution. (b) *Operando* Raman-MS setup for probing the electrode/polyelectrolyte interface in MEA electrolyzer. The cathode was a Cu/QAPEEK (ionomer) GDE, and the anode was a porous IrO_2-coated Ti electrode, with pure water as the anolyte. The right illustration shows the chemical structures of the QAPEEK ionomer and the QAPPT membrane. Both setups were operated at room temperature and ambient pressure in this study.

Figure 2a presents the *in-situ* Raman spectra for CO_2 reduction at the Cu GDE/1 M $KHCO_3$ interface across varying current densities from 50 to 300 mA/cm², obtained using the setup

depicted in Figure 1a. Testing at higher current densities was limited due to interference from gas bubbles, as mentioned above. The obtained spectra are consistent with those reported in the literature,[34,35] displaying some characteristic vibrational bands. The bands at around 280 cm^{-1}, 360 cm^{-1}, and 2060 cm^{-1} correspond to the frustrated rotation, Cu-CO stretching, and C-O stretching of linearly adsorbed $*CO_L$, respectively,[36–38] which is generally considered a key intermediate for CO_2 deep reduction into CH_4 as well as C_2 products (e.g., C_2H_4, C_2H_5OH).[39] The band at 526 cm^{-1} is attributed to surface Cu-OH species.[40,41] The bands at 1015 cm^{-1} and 1070 cm^{-1} correspond to the HCO_3^- and CO_3^{2-}, respectively,[42,43] with their relative intensity reflecting the local pH near the electrode surface. The band at 1386 cm^{-1} can be assigned to the C-O vibration of *COOH intermediate.[44,45] Additionally, the bands at 1600 cm^{-1} and 3000-3600 cm^{-1} are associated with the bending ($\delta(H_2O)$) and stretching (ν(O-H)) vibration of interfacial water, respectively.[46,47]

Figure 2b shows the *operando* Raman spectra for CO_2 reduction at the Cu/QAPEEK (i.e., electrode/polyelectrolyte) interface across current densities ranging from 50 to 700 mA/cm^2, obtained using the MEA setup illustrated in Figure 1b. The peaks marked with asterisks can be assigned to the characteristic signals of QAPEEK ionomer, by referring to its Raman spectrum in Figure S7. The spectra collected differ notably from those in the liquid electrolyte (Figure 2a). Figure 2c-2f highlight the regions with significant spectral differences in Raman spectra acquired at 100 mA/cm^2. Notably, the characteristic bands of $*CO_L$ at 280 cm^{-1}, 360 cm^{-1}, and 2060 cm^{-1} were not detected at the Cu/QAPEEK interface (Figure 2c, 2e). Instead, a band at ~1830 cm^{-1}, corresponding to bridge-absorbed $*CO_B$,[48,49] and an unidentified band near 1945 cm^{-1} (Figure 2b, 2e)—rarely observed for CO_2 reduction on Cu electrodes in conventional liquid electrolytes—were detected. The unidentified band at 1945 cm^{-1} shifted to lower Raman shift positions as the current density increased (i.e., with increasing polarization potential, Figure 2b red dashed line), demonstrating a Stark effect and suggesting that it is associated with an adsorbed species on the electrode surface. Additionally, a broad band appeared at approximately ~460 cm^{-1} (Figure 2c), whose intensity seems to correlate with changes in the 1750~2000 cm^{-1} region ($*CO_B$ and a new, yet-to-be-identified species) as the current density increased (Figure 2b). This band at ~460 cm^{-1} is distinct from both $Cu-CO_L$ and Cu-OH species and likely consists of two different vibrations or species, as indicated by its asymmetric peak

7

shape. Moreover, both the two bands at ~460 cm^{-1} and 1750~2000 cm^{-1} disappeared in Ar atmosphere (Figure S8), suggesting that they are associated with CO_2 reduction intermediates rather than any impurities or decomposition products of the ionomer.
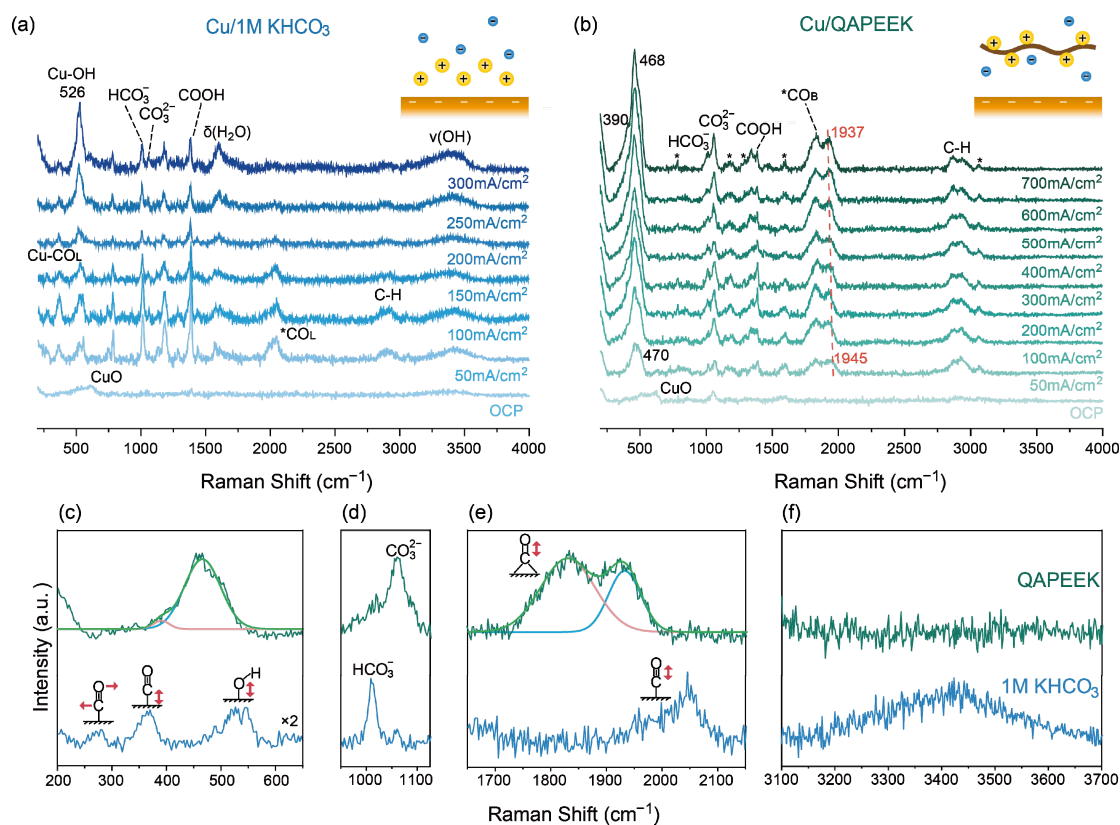

Figure 2. Comparison of the Raman spectra for CO_2 reduction at the electrode/liquid electrolyte and electrode/polyelectrolyte interface. (a) *In-situ* Raman spectra for CO_2 reduction at the Cu/1 M $KHCO_3$ liquid electrolyte interface under varying current densities. (b) *Operando* Raman spectra for CO_2 reduction at the Cu/QAPEEK interface under varying current densities. (c-f) Comparison of Raman spectra in different regions at the electrode/liquid electrolyte interface (Cu/1 M $KHCO_3$, lower blue curves) and electrode/polyelectrolyte interface (Cu/QAPEEK, upper green curves) at 100 mA/cm^2.

In addition, although the bands of HCO_3^- and CO_3^{2-} were still present at the Cu/QAPEEK interface, their relative intensity was reversed compared to those in the liquid electrolyte (Figure 2d). The local pH values for the two systems under different current densities were calculated using the CO_3^{2-}/HCO_3^- integral area ratio and the Henderson-Hasselbalch equation (Figure S9, Note 1),[50] revealing a higher pH at the electrode/polyelectrolyte interface. This phenomenon likely stems from the unique properties of polyelectrolytes compared to liquid electrolytes.

8

Specifically, the movement of anions (e.g., OH^-) is somewhat constrained by the alkaline polyelectrolyte-bounded cations, hindering the rapid transfer of OH^-—generated from CO_2 reduction and water dissociation—away from the electrode surface.

Another significant observation is the complete disappearance of the ν(O-H) band at the Cu/QAPEEK interface (Figure 2b, 2f). This can be attributed to two factors: first, the reduced water content at the electrode/polyelectrolyte interface due to the presence of the hydrophobic backbone of QAPEEK; and second, the preservation of a strong hydrogen bonding network within the water at this interface, due to the inability of the polyelectrolyte-tethered organic cations to form a compact double layer under negative potentials, as found in our previous study.[17] There is a broad consensus that Raman spectroscopy is insensitive to water, but recent research suggests that the disruption of hydrogen bonding network is critical for detecting water vibrations via surface-enhanced Raman spectroscopy.[51] This explains why the ν(O-H) band can be detected at the electrode/liquid electrolyte interface (Cu/1 M $KHCO_3$, Figure 2a), whereas it cannot be detected at the electrode/polyelectrolyte interface (Cu/QAPEEK, Figure 2b).

To identify these specific species and their formation mechanism, as well as examine their relevance to CO_2 reduction at the electrode/polyelectrolyte interface, various CO_2 reduction volatile products, including CO, CH_4, C_2H_4, and C_2H_5OH, were simultaneously monitored in real-time using the *operando* MS technique (Figure 1b), alongside Raman measurement. The yields of these products generally exhibited an increasing trend with rising current densities (Figure 3a). Figure 3b presents the average ion currents of these products at different current densities, while Figure 3c displays the integral areas of the unidentified band at ~1945 cm^{-1}. Notably, as the current density increased, there was a strong correlation between the generation rate of C_2 products (C_2H_4 and C_2H_5OH) and the peak intensity at ~1945 cm^{-1}. Both showed a synchronized changing profile, which was different from the generation rates of CO and CH_4. This suggests that the band at ~1945 cm^{-1} likely corresponds to a key intermediate involved in the C_2 products formation. Furthermore, the correlation between the generation rates of these volatile products and the *CO_B peak intensity is minimal (Figure S10), supporting claims in the literature that *CO_B acts as a surface inactive poisoning species and cannot undergo subsequent reduction.[48]
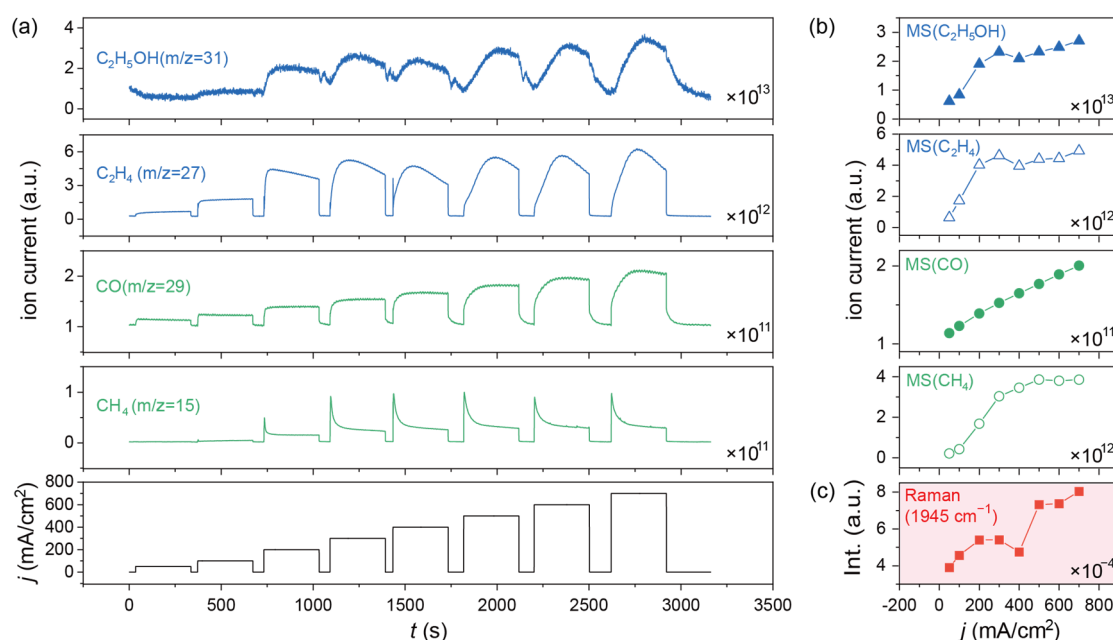
9

Figure 3. *Operando* **MS monitoring of volatile products during CO_2 reduction at the electrode/polyelectrolyte interface.** (a) Variation of MS ionic current for different products (upper) and applied current densities (lower) over time. (b) Average MS ionic current for different products (c) and integral peak area of the Raman band at around 1945 cm^{-1} under varying current densities.

To identify the newly detected species at the electrode/polyelectrolyte interface, we conducted isotopic experiments employing [13]C- and D-labelling (Figure 4a-4c, Figure S11). The $^{12}CO_2/^{13}CO_2$ exchange resulted in a noticeable redshift of the Raman bands at 1945 cm^{-1}, 1834 cm^{-1}, 460 cm^{-1}, and 353 cm^{-1} (Figure 4b, 4c). In contrast, these bands exhibited negligible shifts in the H_2O/D_2O isotope exchange, indicating that the corresponding species contain carbon but no hydrogen. Specifically, the band shift from 1834 cm^{-1} to 1793 cm^{-1} aligns well with the estimated value for $*CO_B$ (Supporting Note 2). For the unidentified band at ~1945 cm^{-1}, which is associated with C_2 products formation, a redshift from 1945 cm^{-1} to 1913 cm^{-1} was observed during the $^{12}CO_2/^{13}CO_2$ exchange. Previous studies have suggested that the vibration bands in the 1900~2000 cm^{-1} range may correspond to two adjacent adsorbed *CO in the co-existence of *OH,[52] multi-bound CO,[53] or *CCO.[54] However, based on the band shift value noted in the isotope experiments, we can rule out the possibility that this band corresponds to surface-adsorbed *CO species (Supporting Note 2). On the other hand, *CCO is often regarded as an intermediate in the conversion of CO_2 to C_2 products. Although it has

10

been referenced in numerous studies related to CO_2 reduction pathways,[55,56] it is rarely detected spectroscopically. Our analysis indicates that both the isotope-induced band shifts from 1945 cm^{-1} to 1913 cm^{-1} and from 460 cm^{-1} to 453 cm^{-1} are consistent well with two vibration modes of the *CCO (Supporting Note 2), and the changes in the integral areas of the two peaks also show a strong correlation as the current density increases (Figure 2b, S12). Moreover, the band at 1945 cm^{-1} is also quite closely matched to that of the CCO molecule in the gas phase.[57,58] According to our further AIMD calculations (Figure S13), the band at 1945 cm^{-1} can be assigned to the asymmetric stretching vibration, while the band at 460 cm^{-1} corresponds to the bending vibration of *CCO.
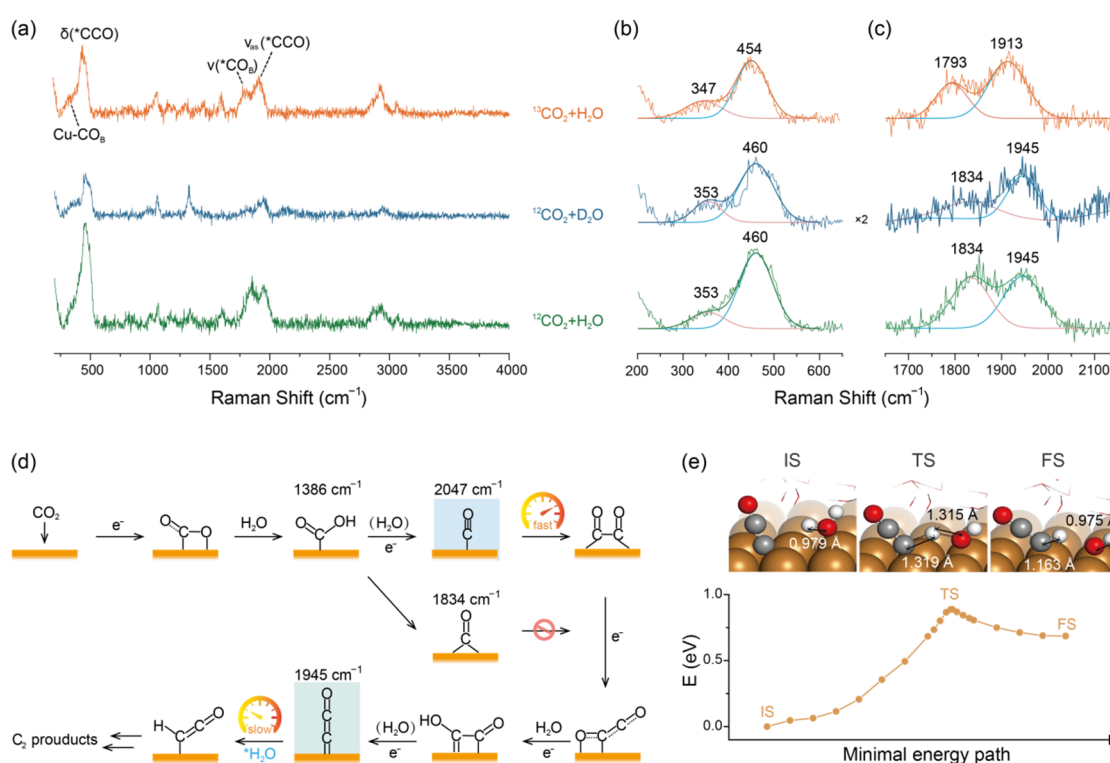

Figure 4. Isotope-exchange *operando* Raman spectroscopy and reaction mechanism. (a) *Operando* Raman spectra for CO_2 reduction at the Cu/QAPEEK interface under 400 mA/cm^2 and different isotope-labeling conditions: $^{13}CO_2$ + H_2O (orange), CO_2 + D_2O (blue), and CO_2 + H_2O (green). The isotope-exchange Raman spectra under various current densities are illustrated in Figure S11. Zoom-in view and peak fitting of the Raman spectra in the regions of 200~650 cm^{-1} (b) and 1650~2150 cm^{-1} (c). (d) Proposed pathways for CO_2 reduction to C_2 products: in which H_2O represents the hydrogenation step where water acts as a reactant (i.e., proton source), and (H_2O) represents the dehydration step where water serves as a product. (e) Protonation process of *CCO through minimal energy path. IS: initial state, TS: transitional state, FS: final state.

Based on the results mentioned above and the CO_2 reduction pathways hypothesized in previous studies,[31] the unusual CO_2 reduction reaction pathways at the electrode/polyelectrolyte interface (i.e., Cu/QAPEEK) can be schematically illustrated in Figure 4d. The high local pH at this interface (Figure S9), generally believed to facilitate C-C coupling,[59,60] leads to the rapid consumption and conversion of active $*CO_L$. This explains why $*CO_L$ is not observed in *operando* Raman spectra. Moreover, in the preceding steps for *CCO generation, protonation primarily occurs at the highly electronegative oxygen ($O^{\delta-}$) site rather than at carbon ($C^{\delta+}$), for example, as seen in the step of *COOH formation. Due to the restricted mobility of polyelectrolyte-tethered organic cations, a rigid hydrogen bonding network is maintained at the electrode/polyelectrolyte interface under negative potentials, with a high proportion of strongly hydrogen-bonded water (*sh*-H_2O). It is reasonable to infer that the $H^{\delta+}$ in *sh*-H_2O can readily interact with the $O^{\delta-}$ in these oxygen-containing intermediates, facilitating direct protonation with interfacial water via the Eley-Rideal mechanism.[61] However, for the further conversion of *CCO, the protonation of α-C to form *CHCO is thermodynamically more favorable.[62]

To elucidate the protonation process of *CCO, we conducted density functional theory (DFT) calculations. The calculations demonstrate that the protonation of α-C atom via the Eley-Rideal mechanism—where *CCO reacts with dangling water molecules above the electrode surface—is not feasible, restricted by the substantial spatial separation between them. Instead, due to the proximity of the α-C atom to the electrode surface, the only viable pathway for this protonation process follows the Langmuir-Hinshelwood mechanism, where the reaction occurs with surface-adsorbed water ($*H_2O$, Figure S14). Nonetheless, this pathway still needs to overcome a relatively high transition-state energy barrier of 0.89 eV (Figure 4e). In addition, due to the low water content and the constraint imposed by the rigid hydrogen bonding network at the electrode/polyelectrolyte interface, the transport and adsorption of water molecules onto the electrode surface are significantly limited. Consequently, the conversion rate of *CCO to *CHCO is relatively slow, allowing the Raman detection of the *CCO intermediate. This also explains the absence of Cu-OH species (526 cm^{-1}) at the electrode/polyelectrolyte interface (Cu/QAPEEK, Figure 2b, 2c), in stark contrast to the electrode/liquid electrolyte interface, as observed in our study (Cu/1 M $KHCO_3$, Figure 2a, 2c) and supported by the general findings

in the literature.[34,63,64] This is because surface *OH (i.e., Cu-OH) is another product from the Langmuir-Hinshelwood hydrogenation reaction with surface-adsorbed water (*H_2O, Figure 4e upper), and thus its formation is similarly hindered. Overall, the distinct electrode/polyelectrolyte interfacial structure shifts the rate-determining step from the usual C-C coupling to the *CCO hydrogenation in the conversion of CO_2 to C_2 products.

Conclusions

In summary, we have investigated the CO_2 reduction mechanism at the electrode/polyelectrolyte interface within a practical MEA electrolyzer by combining *operando* Raman and MS analyses. We successfully captured direct spectroscopic evidence of a key *CCO intermediate for C_2 products formation, which was further verified through [13]C- and D-isotopic substitution experiments as well as AIMD calculations. Notably, the *CCO intermediate has been rarely detected in previous studies on CO_2 reduction in conventional liquid electrolytes. This observation is due to the distinct structural characteristics of the electrode/polyelectrolyte interface, including a relatively high local pH, lower water content, and a more rigid hydrogen bonding network in the interfacial water. These features favor the Eley-Rideal type hydrogenation and disfavor the Langmuir-Hinshelwood type hydrogenation in CO_2 reduction, thus promoting the conversion of surface-active *CO_L to *CCO while limiting its further protonation. These findings can not only facilitate the design of efficient electrocatalytic interfaces in practical MEA electrolyzers for CO_2 and pure water co-electrolysis, but also highlight the importance of developing *operando* spectroscopic methods for studying interfacial catalysis under MEA working conditions. Further efforts can be made to introduce a stable and reliable reference electrode into the MEA device, in order to probe changes in interfacial species at different electrode potentials, rather than just observing their variations relative to current densities. Although some studies have attempted this, eliminating the measurement errors resulting from non-uniform current/potential distributions still poses a challenge.[65,66]

13

Data Availability

All data supporting the findings of this study are available within the paper and Supporting Information files.

14

References

[1] S. Lee, J. G. Seong, Y. Jo, S.-J. Hwang, G. Gwak, Y. Park, Y. C. Kim, K. H. Lim, H.-Y. Park, J. H. Jang, H.-J. Kim, S.-W. Nam, S. Y. Lee, *Nat. Energy* **2024**, *9*, 849–861.

[2] B. Peng, Z. Liu, L. Sementa, Q. Jia, Q. Sun, C. U. Segre, E. Liu, M. Xu, Y.-H. Tsai, X. Yan, Z. Zhao, J. Huang, X. Pan, X. Duan, A. Fortunelli, Y. Huang, *Nat. Catal.* **2024**, *7*, 818–828.

[3] A. Li, S. Kong, K. Adachi, H. Ooka, K. Fushimi, Q. Jiang, H. Ofuchi, S. Hamamoto, M. Oura, K. Higashi, T. Kaneko, T. Uruga, N. Kawamura, D. Hashizume, R. Nakamura, *Science* **2024**, *384*, 666–670.

[4] X. Chen, X. Li, Y. Peng, H. Yang, Y. Tong, M. -Sadeeq Balogun, Y. Huang, *Adv. Funct. Mater.* **2025**, *35*, 2416091.

[5] Z.-H. Zhao, J.-R. Huang, D.-S. Huang, H.-L. Zhu, P.-Q. Liao, X.-M. Chen, *J. Am. Chem. Soc.* **2024**, *146*, 14349–14356.

[6] Q. Zhu, C. L. Rooney, H. Shema, C. Zeng, J. A. Panetier, E. Gross, H. Wang, L. R. Baker, *Nat. Catal.* **2024**, *7*, 987–999.

[7] E. Pastor, Z. Lian, L. Xia, D. Ecija, J. R. Galán-Mascarós, S. Barja, S. Giménez, J. Arbiol, N. López, F. P. García De Arquer, *Nat. Rev. Chem.* **2024**, *8*, 159–178.

[8] Chinese Society of Electrochemistry, *J. Electrochem.* **2024**, *30(1)*, 2024121.

[9] N. Heidary, K. H. Ly, N. Kornienko, *Nano Lett.* **2019**, *19*, 4817–4826.

[10] Y.-Z. Zhu, K. Wang, S.-S. Zheng, H.-J. Wang, J.-C. Dong, J.-F. Li, *Acta Phys. Chim. Sin.* **2023**, *40*, 2304040.

[11] Y.-H. Wang, S. Zheng, W.-M. Yang, R.-Y. Zhou, Q.-F. He, P. Radjenovic, J.-C. Dong, S. Li, J. Zheng, Z.-L. Yang, G. Attard, F. Pan, Z.-Q. Tian, J.-F. Li, *Nature* **2021**, *600*, 81–85.

[12] E. P. Delmo, Y. Wang, Y. Song, S. Zhu, H. Zhang, H. Xu, T. Li, J. Jang, Y. Kwon, Y. Wang, M. Shao, *J. Am. Chem. Soc.* **2024**, *146*, 1935–1945.

[13] Y. Wang, J. Huang, Y. Chen, H. Yang, K.-H. Ye, Y. Huang, *J. Colloid Interface Sci.* **2024**, *672*, 12–20.

[14] Y. Yang, P. Li, X. Zheng, W. Sun, S. X. Dou, T. Ma, H. Pan, *Chem. Soc. Rev.* **2022**, *51*, 9620–9693.

15

[15] C. Chen, Y. Li, P. Yang, *Joule* **2021**, *5*, 737–742.

[16] Z. Gao, L. Xue, X. Hu, J. Yin, L. Xiao, G. Wang, J. Lu, L. Zhuang, *Electrochim. Acta* **2023**, *458*, 142509.

[17] Z. Mi, T. Wang, L. Xiao, G. Wang, L. Zhuang, *J. Am. Chem. Soc.* **2024**, *146*, 17377–17383.

[18] H. Li, K. Jiang, S.-Z. Zou, W.-B. Cai, *Chin. J. Catal.* **2022**, *43*, 2772–2791.

[19] Z. Tao, A. J. Pearce, J. M. Mayer, H. Wang, *J. Am. Chem. Soc.* **2022**, *144*, 8641–8648.

[20] R. E. Vos, K. E. Kolmeijer, T. S. Jacobs, W. Van Der Stam, B. M. Weckhuysen, M. T. M. Koper, *ACS Catal.* **2023**, *13*, 8080–8091.

[21] L. Huang, G. Gao, C. Yang, X.-Y. Li, R. K. Miao, Y. Xue, K. Xie, P. Ou, C. T. Yavuz, Y. Han, G. Magnotti, D. Sinton, E. H. Sargent, X. Lu, *Nat. Commun.* **2023**, *14*, 2958.

[22] Y. Wang, Y. Yang, S. Jia, X. Wang, K. Lyu, Y. Peng, H. Zheng, X. Wei, H. Ren, L. Xiao, J. Wang, D. A. Muller, H. D. Abruña, B. J. Hwang, J. Lu, L. Zhuang, *Nat. Commun.* **2019**, *10*, 1506.

[23] M. Bogar, Y. Yakovlev, S. Pollastri, R. Biagi, H. Amenitsch, R. Taccani, I. Matolínová, *J. Power Sources* **2024**, *615*, 235070.

[24] Y. Wen, C. Liu, R. Huang, H. Zhang, X. Li, F. P. García De Arquer, Z. Liu, Y. Li, B. Zhang, *Nat. Commun.* **2022**, *13*, 4871.

[25] H. S. Casalongue, S. Kaya, V. Viswanathan, D. J. Miller, D. Friebel, H. A. Hansen, J. K. Nørskov, A. Nilsson, H. Ogasawara, *Nat. Commun.* **2013**, *4*, 2817.

[26] J. Du, J. Ye, C. Yang, C. Qiu, N. Fang, Y. Wang, Z. Zhou, S. Sun, *Angew. Chem. Int. Ed.* **2025**, e202503868.

[27] K. Kunimatsu, T. Yoda, D. A. Tryk, H. Uchida, M. Watanabe, *Phys Chem Chem Phys* **2010**, *12*, 621–629.

[28] N. Loupe, J. Doan, R. Cruse, C. A. DiMarzio, E. S. Smotkin, *Electrochim. Acta* **2018**, *283*, 1079–1086.

[29] I. Kendrick, J. Fore, J. Doan, N. Loupe, A. Vong, N. Dimakis, M. Diem, E. S. Smotkin, *J. Electrochem. Soc.* **2016**, *163*, H3152–H3159.

[30] H. Li, P. Wei, D. Gao, G. Wang, *Curr. Opin. Green Sustain. Chem.* **2022**, *34*, 100589.

[31] R. Kortlever, J. Shen, K. J. P. Schouten, F. Calle-Vallejo, M. T. M. Koper, *J. Phys. Chem. Lett.* **2015**, *6*, 4073–4082.

16

[32] J. F. Li, X. D. Tian, S. B. Li, J. R. Anema, Z. L. Yang, Y. Ding, Y. F. Wu, Y. M. Zeng, Q. Z. Chen, B. Ren, Z. L. Wang, Z. Q. Tian, *Nat. Protoc.* **2013**, *8*, 52–65.

[33] P. Zhu, C. Xia, C.-Y. Liu, K. Jiang, G. Gao, X. Zhang, Y. Xia, Y. Lei, H. N. Alshareef, T. P. Senftle, H. Wang, *Proc. Natl. Acad. Sci.* **2021**, *118*, e2010868118.

[34] Y. Zhao, X.-G. Zhang, N. Bodappa, W.-M. Yang, Q. Liang, P. M. Radjenovica, Y.-H. Wang, Y.-J. Zhang, J.-C. Dong, Z.-Q. Tian, J.-F. Li, *Energy Environ. Sci.* **2022**, *15*, 3968–3977.

[35] J. de Ruiter, H. An, L. Wu, Z. Gijsberg, S. Yang, T. Hartman, B. M. Weckhuysen, W. van der Stam, *J. Am. Chem. Soc.* **2022**, *144*, 15047–15058.

[36] C. J. Hirschmugl, G. P. Williams, F. M. Hoffmann, Y. J. Chabal, *Phys. Rev. Lett.* **1990**, *65*, 480–483.

[37] W. Akemann, A. Otto, *J. Raman Spectrosc.* **1991**, *22*, 797–803.

[38] C. M. Gunathunge, X. Li, J. Li, R. P. Hicks, V. J. Ovalle, M. M. Waegele, *J. Phys. Chem. C* **2017**, *121*, 12337–12344.

[39] K. J. P. Schouten, Y. Kwon, C. J. M. Van Der Ham, Z. Qin, M. T. M. Koper, *Chem. Sci.* **2011**, *2*, 1902.

[40] G. Niaura, *Electrochim. Acta* **2000**, *45*, 3507–3519.

[41] M. Moradzaman, G. Mul, *ChemElectroChem* **2021**, *8*, 1478–1485.

[42] H. King, T. Geisler, *Minerals* **2018**, *8*, 158.

[43] S. Jiang, K. Klingan, C. Pasquini, H. Dau, *J. Chem. Phys.* **2019**, *150*, 041718.

[44] W. Shan, R. Liu, H. Zhao, Z. He, Y. Lai, S. Li, G. He, J. Liu, *ACS Nano.* **2020**, *14*, 11363–11372.

[45] N. J. Firet, W. A. Smith, *ACS Catal.* **2017**, *7*, 606–612.

[46] J. Schaefer, E. H. G. Backus, Y. Nagata, M. Bonn, *J. Phys. Chem. Lett.* **2016**, *7*, 4591–4595.

[47] C.-Y. Li, J.-B. Le, Y.-H. Wang, S. Chen, Z.-L. Yang, J.-F. Li, J. Cheng, Z.-Q. Tian, *Nat. Mater.* **2019**, *18*, 697–701.

[48] C. M. Gunathunge, V. J. Ovalle, Y. Li, M. J. Janik, M. M. Waegele, *ACS Catal.* **2018**, *8*, 7507–7516.

[49] J. Salimon, R. M. Hernández-Romero, M. Kalaji, *J. Electroanal. Chem.* **2002**, *538–539*, 99–108.

[50] D. A. Henckel, M. J. Counihan, H. E. Holmes, X. Chen, U. O. Nwabara, S. Verma, J. Rodríguez-López, P. J. A. Kenis, A. A. Gewirth, *ACS Catal.* **2021**, *11*, 255–263.

[51] R. Kamimura, S. Maeda, T. Hayashi, K. Motobayashi, K. Ikeda, *J. Am. Chem. Soc.* **2024**, *146*, 22327–22334.

[52] G. Iijima, T. Inomata, H. Yamaguchi, M. Ito, H. Masuda, *ACS Catal.* **2019**, *9*, 6305–6319.

[53] H. An, J. De Ruiter, L. Wu, S. Yang, F. Meirer, W. Van Der Stam, B. M. Weckhuysen, *JACS Au* **2023**, *3*, 1890–1901.

[54] F. Shao, J. K. Wong, Q. H. Low, M. Iannuzzi, J. Li, J. Lan, *Proc. Natl. Acad. Sci.* **2022**, *119*, e2118166119.

[55] F. Calle-Vallejo, M. T. M. Koper, *Angew. Chem. Int. Ed.* **2013**, *52*, 7282–7285.

[56] T. Cheng, H. Xiao, W. A. Goddard, *Proc. Natl. Acad. Sci.* **2017**, *114*, 1795–1800.

[57] M. E. Jacox, D. E. Milligan, N. G. Moll, W. E. Thompson, *J. Chem. Phys.* **1965**, *43*, 3734–3746.

[58] N. Moazzen-Ahmadi, D. W. D. Sandilands, R. T. Boeré, *Chem. Phys. Lett.* **1997**, *265*, 563–572.

[59] Z. Wang, Y. Li, X. Zhao, S. Chen, Q. Nian, X. Luo, J. Fan, D. Ruan, B.-Q. Xiong, X. Ren, *J. Am. Chem. Soc.* **2023**, *145*, 6339–6348.

[60] C.-T. Dinh, T. Burdyny, M. G. Kibria, A. Seifitokaldani, C. M. Gabardo, F. P. García De Arquer, A. Kiani, J. P. Edwards, P. De Luna, O. S. Bushuyev, C. Zou, R. Quintero-Bermudez, Y. Pang, D. Sinton, E. H. Sargent, *Science* **2018**, *360*, 783–787.

[61] C. Becker, From Langmuir to Ertl: The "Nobel" History of the Surface Science Approach to Heterogeneous Catalysis in *Encycl. Interfacial Chem.*, Amsterdam, Elsevier, **2018**, pp. 99–106.

[62] H.-J. Peng, M. T. Tang, J. Halldin Stenlid, X. Liu, F. Abild-Pedersen, *Nat. Commun.* **2022**, *13*, 1399.

[63] F. Shao, Z. Xia, F. You, J. K. Wong, Q. H. Low, H. Xiao, B. S. Yeo, *Angew. Chem. Int. Ed.* **2023**, *62*, e202214210.

[64] N. Bodappa, M. Su, Y. Zhao, J.-B. Le, W.-M. Yang, P. Radjenovic, J.-C. Dong, J. Cheng, Z.-Q. Tian, J.-F. Li, *J. Am. Chem. Soc.* **2019**, *141*, 12192–12196.

[65] W. He, T. V. Nguyen, *J. Electrochem. Soc.* **2004**, *151*, A185.

18

[66] K. U. Hansen, L. H. Cherniack, F. Jiao, *ACS Energy Lett.* **2022**, *7*, 4504–4511.

19

Table of Contents
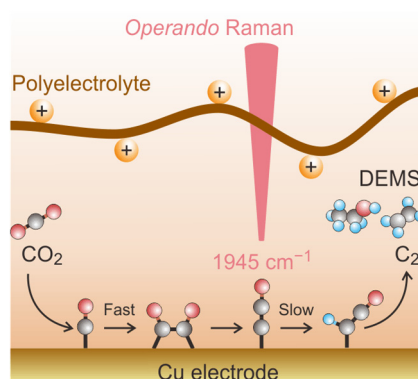
The catalytic mechanism of CO_2 reduction at the electrode/polyelectrolyte interface was investigated using *operando* Raman spectroscopy and differential electrochemical mass spectrometry. Under the practical working conditions of the membrane electrode assembly (MEA) electrolyzer for CO_2 and pure water co-electrolysis, the rate-determining step for CO_2-to-C_2 conversion was found to shift from C-C coupling to the subsequent *CCO hydrogenation.

20